Supplementary Information (SI)

Manganese-based A-site high-entropy perovskite oxide for solar thermochemical hydrogen production

Cijie Liu,‡[a] Dawei Zhang,‡[b] Wei Li,*[a] Jamie A. Trindell,[c] Keith A. King,[c] Sean R. Bishop,[d] Joshua D. Sugar,[c] Anthony H. McDaniel,[c] Andrew I. Smith,[d] Perla A. Salinas,[d] Eric N. Coker,[d] Arielle L. Clauser,[c] Murugesan Velayutham,[ef] Joerg C. Neuefeind,[g] Jingjing Yang,[b] Héctor A. De Santiago,[a] Liang Ma,[a] Yi Wang,[a] Qiang Wang,[h] Wenyuan Li,[i] Qingsong Wang,[j] Qingyuan Li,[a] Hanchen Tian,[a] Ha Ngoc Ngan Tran,[i] Xuemei Li,[i] Brandon Robinson,[i] Angela M. Deibel,[a] Gregory Collins,[a] Nhat Anh Thieu,[a] Jianli Hu,[i] Valery V. Khramtsov,[ef] Jian Luo,*[bk] and Xingbo Liu*[a]

[a] Department of Mechanical and Aerospace Engineering, Benjamin M. Statler College of Engineering and Mineral Resources, West Virginia University, Morgantown, WV 26506, USA. E-mail: wei.li@mail.wvu.edu; xingbo.liu@mail.wvu.edu

[b] Program of Materials Science and Engineering, University of California San Diego, La Jolla, CA 92093, USA

[c] Sandia National Laboratories, Livermore, CA 94551, USA

[d] Sandia National Laboratories, Albuquerque, NM 87123, USA

[e] In Vivo Multifunctional Magnetic Resonance center, Robert C. Byrd Health Sciences Center, West Virginia University, Morgantown, WV 26506, USA

[f] Department of Biochemistry and Molecular Medicine, School of Medicine, West Virginia University, Morgantown, WV 26506, USA

[g] Chemical and Engineering Materials Division, Oak Ridge National Laboratory, Oak Ridge, TN 37831, USA

[h] Shared Research Facilities, West Virginia University, Morgantown, WV 26506, USA

[i] Department of Chemical and Biomedical Engineering, Benjamin M. Statler College of Engineering and Mineral Resources, West Virginia University, Morgantown, WV 26506, USA

[j] Bavarian Center for Battery Technology (BayBatt), Department of Chemistry, University of Bayreuth, Universitätsstrasse 30, 95447 Bayreuth, Germany

[k] Department of Nano and Chemical Engineering, University of California San Diego, La Jolla, CA 92093, USA. E-mail: jluo@alum.mit.edu

‡These authors (C.L. and D.Z.) contributed equally to this work.

*Corresponding authors

Section I. Supplemental Experimental Details

1.1 Material characterization

Scanning electron microscopy (SEM, FEI Apreo) and energy-dispersive X-ray (EDX, Oxford N-MAX) spectroscopy were used to probe the surface morphology, particle size, and elemental distributions of "x" samples. Focused ion beam (FIB) transmission electron microscopy (TEM) lamella was prepared for Scanning (S)TEM analysis using a FEI Scios DualBeam. Raman spectra were acquired by the RENISHAW INVIA Raman spectrometer (Renishaw) with a laser excitation wavelength of 785 nm. Probe-corrected high-angle annular dark-field (HAADF) STEM, energy-dispersive X-ray (EDX) spectroscopy, and *in-situ* STEM electron energy loss spectroscopy (EELS) were used to observe valence change in real time.

1.2 Temperature Programmed Reduction experiment:[1]

The results of thermogravimetric measurements for samples LS21_Mn and LPNGSB_Mn are presented in **Figure S4**. The value of δ was calculated using the formula:

$$\delta = \Delta m_{sample} \frac{M_{sample}}{m_{sample} * M_O} \quad (1)$$

where m_{sample} is the initial weight of the sample, Δm_{sample} is the amount of weight loss at equilibrium, M_{sample} and M_O are the molar masses of the sample and an oxygen atom, respectively.

1.3 Electrical Conductivity Relaxation Experiment (ECR):

The kinetic parameters of the perovskite-type oxide were measured using Electrical Conductivity Relaxation (ECR) under specific test conditions. Firstly, a dense pellet was required to obtain a reliable relaxation curve since high porosity will promote the process of gas entering the pore to change the relaxation curve. The finer powder is beneficial for making dense pellets. To produce finer powders, we utilized the solid-state synthesis method (as described in 2.2 Materials synthesis) and subjected the resulting powder to two rounds of ball milling using a High-Energy Ball Mill (HEBM) to produce a finer powder. Next, 1.1g of the finer powder was added to an agate mortar along with Polyvinyl Butyral (PVB, 10% vol, 0.55mL) as a binder, and anhydrous ethanol as a diluent. The mixture was then pestled for about an hour to evaporate ethanol before being placed in the oven for 5-10 minutes to remove the remaining ethanol. The resulting mixture was then passed through a sieve (125 microns) to separate big

particles and make the sample finer and uniform. After sieving, the sample was placed in a square die (L:12.7mm) and compressed under a pressure of 195 MPa for 20 seconds. The compressed pellet was then placed on a platinum film-covered crucible with some powder in the middle of the Pt film and compressed pellet to counter the loss of element evaporation induced by high temperature. The pellet was then placed in a muffle furnace at 1400 °C for 6 hours with a heating and cooling rate of 5 °C min^{-1} under an airflow. SEM characterization was used to observe the morphology of the baked sample (**Figure S15**). Based on the observation, the dense pellet was smoothed using sandpapers (1000 grit), cut into two rectangular bars using a cutter, and two golden wires were then twined on both sides of the rectangular bar. Golden pulp was used to join the wires for conductivity. Subsequently, the rectangular bar was dried in an oven for 10-15 minutes, after which it was placed in a furnace at 900 °C for 30 minutes under an air atmosphere to remove any potential interferences or contaminants. The ECR test was conducted at a constant current of 0.01A and 900 °C by the auto lab (AUT85484, Nova 1.11). After that, the acquired relaxation curve was fitted by Matlab. The ratio of K_s (oxygen surface exchange) to D (bulk diffusion) is defined as the critical length (L_c) and qualitatively described the relative control of transport, either by bulk diffusion or surface exchange as follows,[2]

$$L = \frac{a}{Lc} = \frac{aK}{D} \quad (2)$$

where a represents the semi-thickness of the pellet sample being tested in a diffusion solution. When the value of 'L' falls between 0.1 and 10, it is indicative of the oxygen transport process being governed by combined controls by bulk diffusion and surface exchange.[2] In our case, with the particle size of approximately 20 μm, L is lower than 0.1, suggesting that K_s should be given priority in considerations.

1.4 The calculation of the steam-to-hydrogen conversion

The steam-to-hydrogen conversion percentage is calculated by dividing the moles of hydrogen produced by the moles of steam consumed.

$$\text{Steam - to - Hydrogen Conversion Percentage} = \frac{\text{Moles of Hydrogen Produced}}{\text{Moles of Steam Consumed}} \quad (3)$$

The flow rate of steam is 200 sccm, so the moles of steam consumed can be calculated by Eq. (4):

$$PV = nRT \quad (4)$$

Taking the steam-to-hydrogen conversion of C1-LPNGSB_Mn-P1 for example: The

consumed mole of steam is 0.1785 mol. The moles of hydrogen produced can be acquired by the quantity of a component that contains 21.8 mmol mol_{oxide}^{-1} in 0.1 grams of an oxide, where the molar mass of the oxide is 237.3044 g mol^{-1}. The moles of hydrogen produced are 7.98×10^{-4} moles. The steam-to-hydrogen conversion is 0.45%.

1.5 Two-step Thermochemical Water Splitting tested in SNL.

The hydrogen production of LPNGSB_Mn and LS21_Mn was measured at Sandia National Lab using different protocols. **Table S4** shows the details of the experimental protocols. **Figure S10** displays the molar hydrogen production rate with time for LPNGSB_Mn and LS21_Mn. In addition, the high-conversion (the molar ratio of H_2O and H_2 is 1000:1) water-splitting cycles for LPNGSB_Mn were also investigated, as shown in **Figure S12**.

Section II. Supplemental Figures and Tables

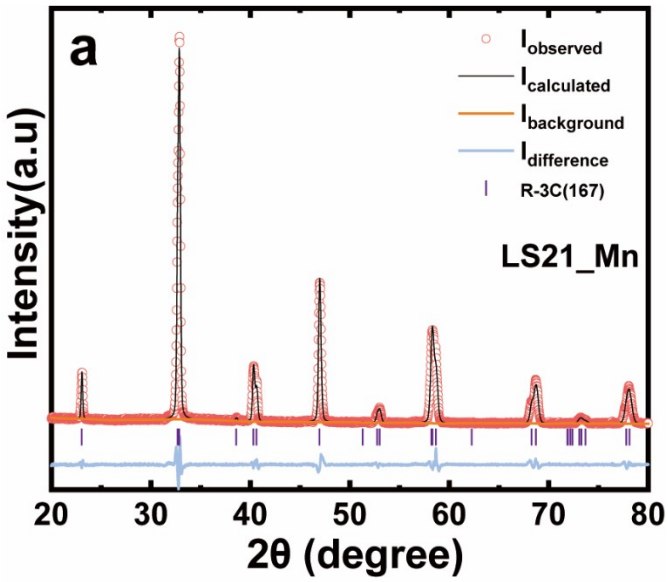

Figure S1 Rietveld-refined powder X-ray diffraction (XRD) pattern for synthesized LS21_Mn. The observed intensity, calculated intensity, and the difference between $I_{observed}$ and $I_{calculated}$ patterns are represented by red hollow circles, black lines, and light blue curves, respectively. The purple vertical lines indicate the calculated Bragg positions ascribed to the rhombohedral structure (with a space group of $R\bar{3}C$).

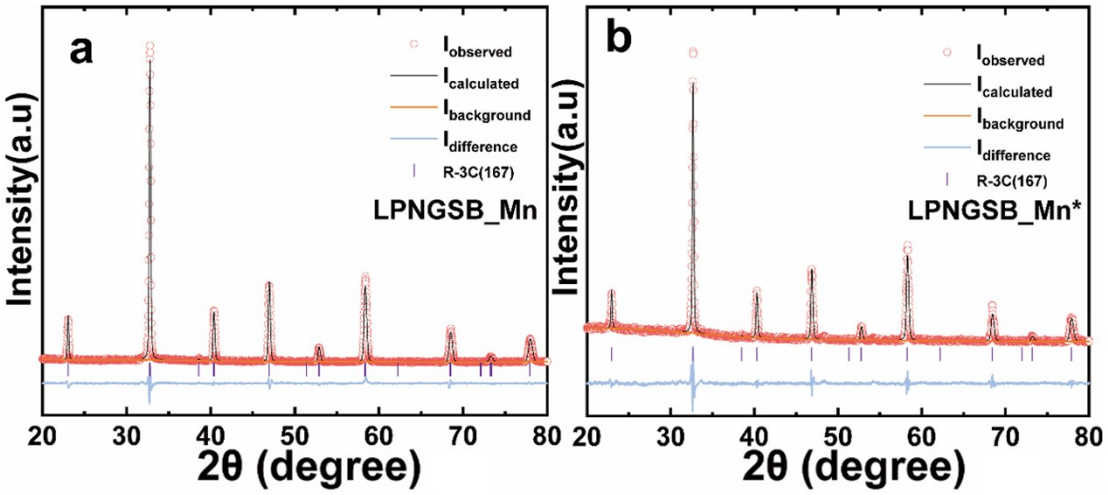

Figure S2 (a-b) Rietveld refined powder X-ray diffraction (XRD) patterns for synthesized LPNGSB_Mn and LPNGSB_Mn*. symbol* represents 50-cycled LPNGSB_Mn sample.

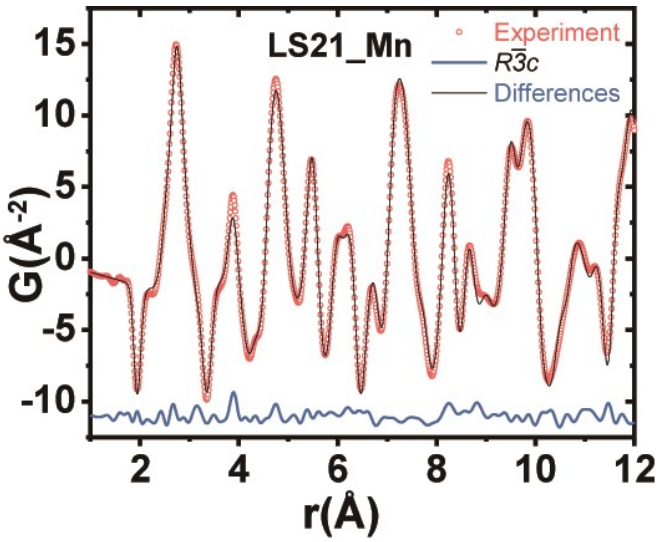

Figure S3 The resulting PDF, $G(r)$, is shown as red symbols. The best-fit Pair Distribution Function (PDF) from the R$\bar{3}$c structural model is plotted in red, while a different curve is shown in blue.

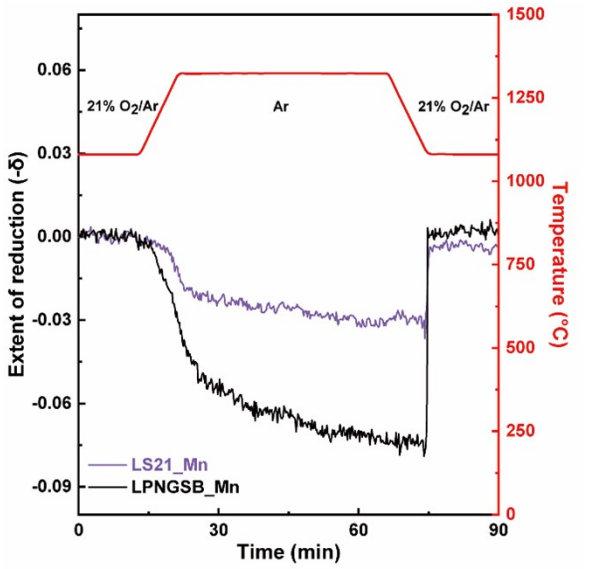

Figure S4 Temperature Programmed Reduction experiment shows the reversibility and the extent of reduction (δ) for synthesized oxides. Oxidation in 21% oxygen at 1100 °C and reduction at 1350 °C for 45 min in UHP argon.

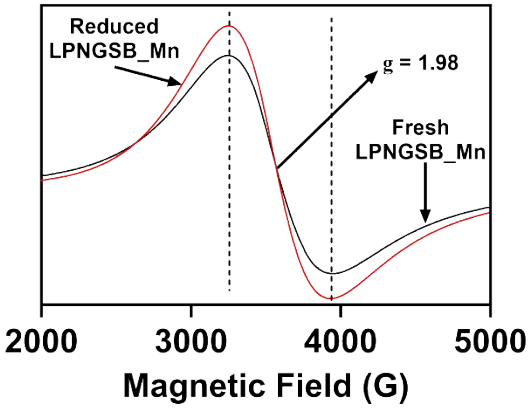

Figure S5 Room temperature X-band EPR spectra of fresh LPNGSB_Mn and reduced LPNGSB_Mn. EPR instrument settings are given in the Experimental section in the main text. The linewidth (ΔH_{pp}) value was calculated from the maximum and minimum values of the peak/signal. The vertical dotted lines are extended from the peaks of the thermally reduced sample spectrum for clarity.

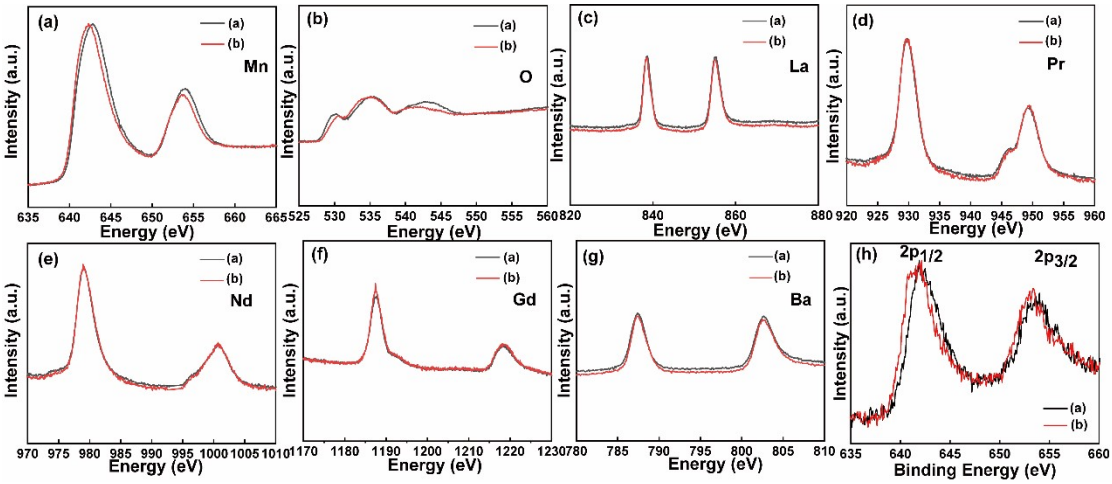

Figure S6 STEM-EELS results of LPNGSB_Mn showing the (a) Mn L-edge, (b) O K-edge, (c) La L-edge, (d) Pr L-edge, (e) Nd L-edge, (f) Gd L-edge, (g) Ba L-edge. (h) the Mn2p core level X-ray photoelectron spectrum (XPS) of LPNGSB_Mn. The Mn peak shows the shift. In panel a-g, the black curve (sub-label "(a)") and red curve (sub-label "(b)") represents the LPNGSB_Mn at 25 °C and LPNGSB at 700 °C, respectively. In panel h, the black curve (sub-label "(a)") and red curve (sub-label "(b)") represents the Fresh-LPNGSB_Mn and LPNGSB after being reduced in Ultra-Pure Nitrogen at 1350 °C for 2h, respectively.

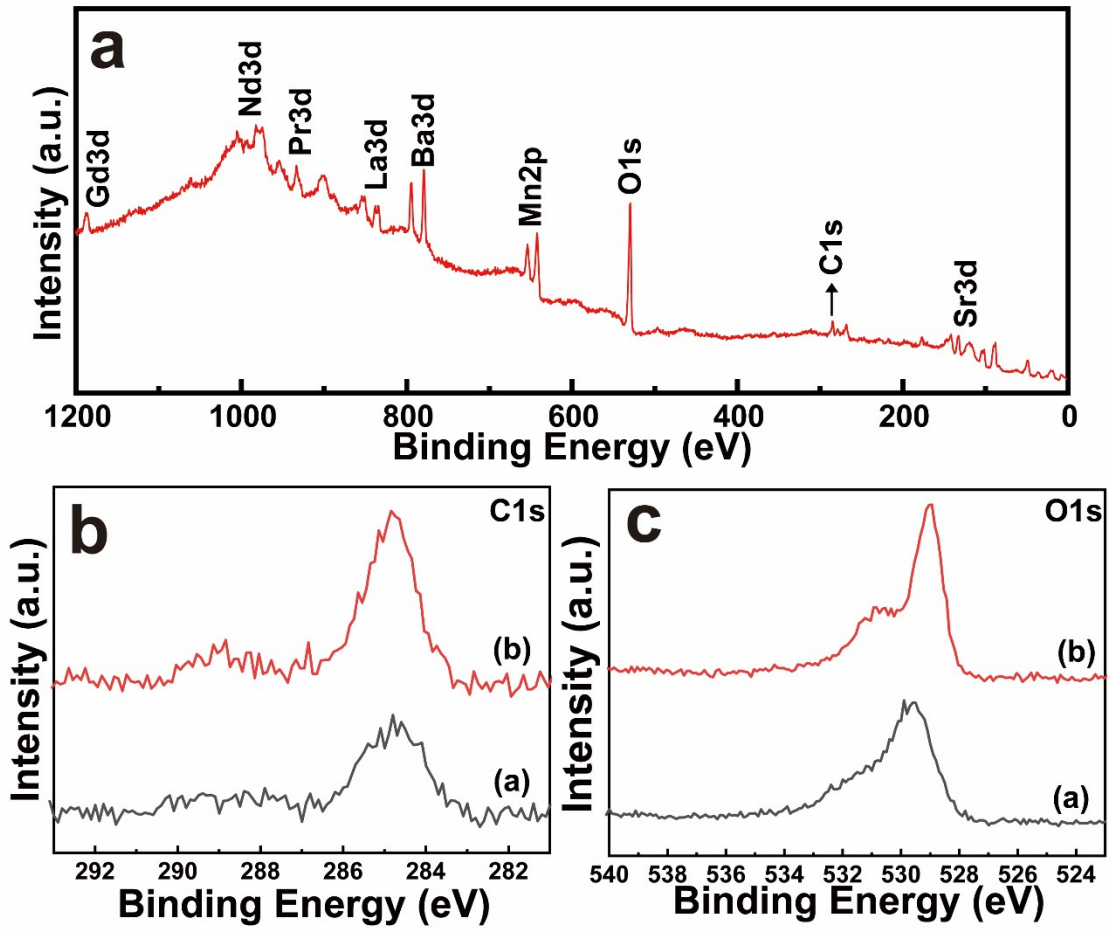

Figure S7 (a) The X-ray Photoelectron Spectroscopy (XPS) survey scan of LPNGSB_Mn (b) The detailed C1s XPS spectrum of LPNGSB_Mn, and (c) The detailed O1s XPS spectrum of LPNGSB_Mn. In panel b and c, the black curve (sub-label "(a)") and red curve (sub-label "(b)") represents the Fresh-LPNGSB_Mn and LPNGSB after being reduced in Ultra-Pure Nitrogen at 1350 °C for 2h, respectively.

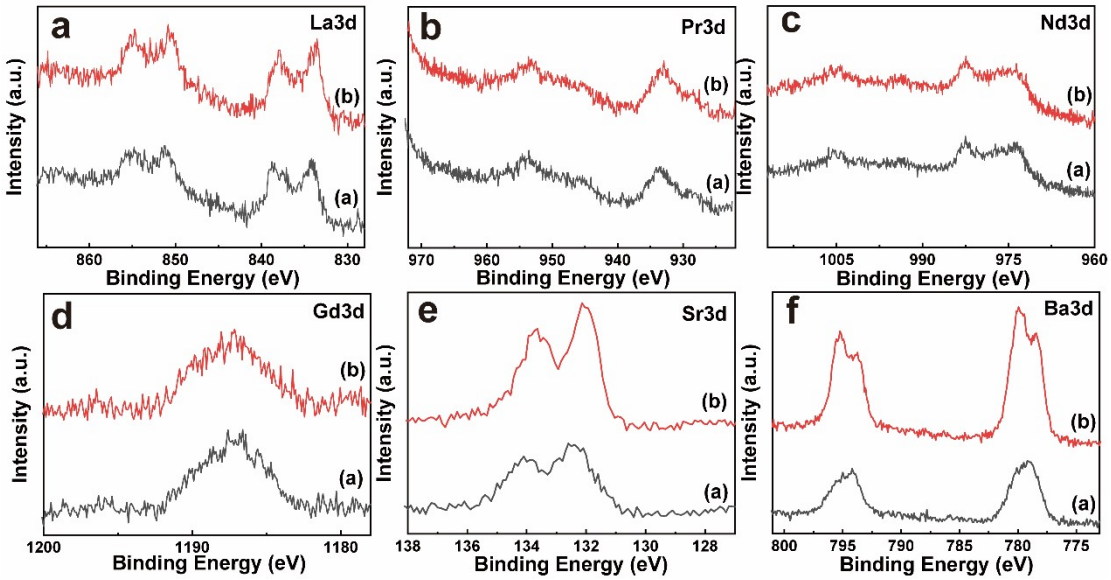

Figure S8 (a) The La3d, (b) the Pr3d, (c) the Nd3d, (d) the Gd3d, (e) the Sr3d, and (f) the Ba3d core level X-ray photoelectron spectrum of LPNGSB_Mn. The black curve (sub-label "(a)") and red curve (sub-label "(b)") represents the Fresh-LPNGSB_Mn and LPNGSB after being reduced in Ultra-Pure Nitrogen at 1350 °C for 2h, respectively.

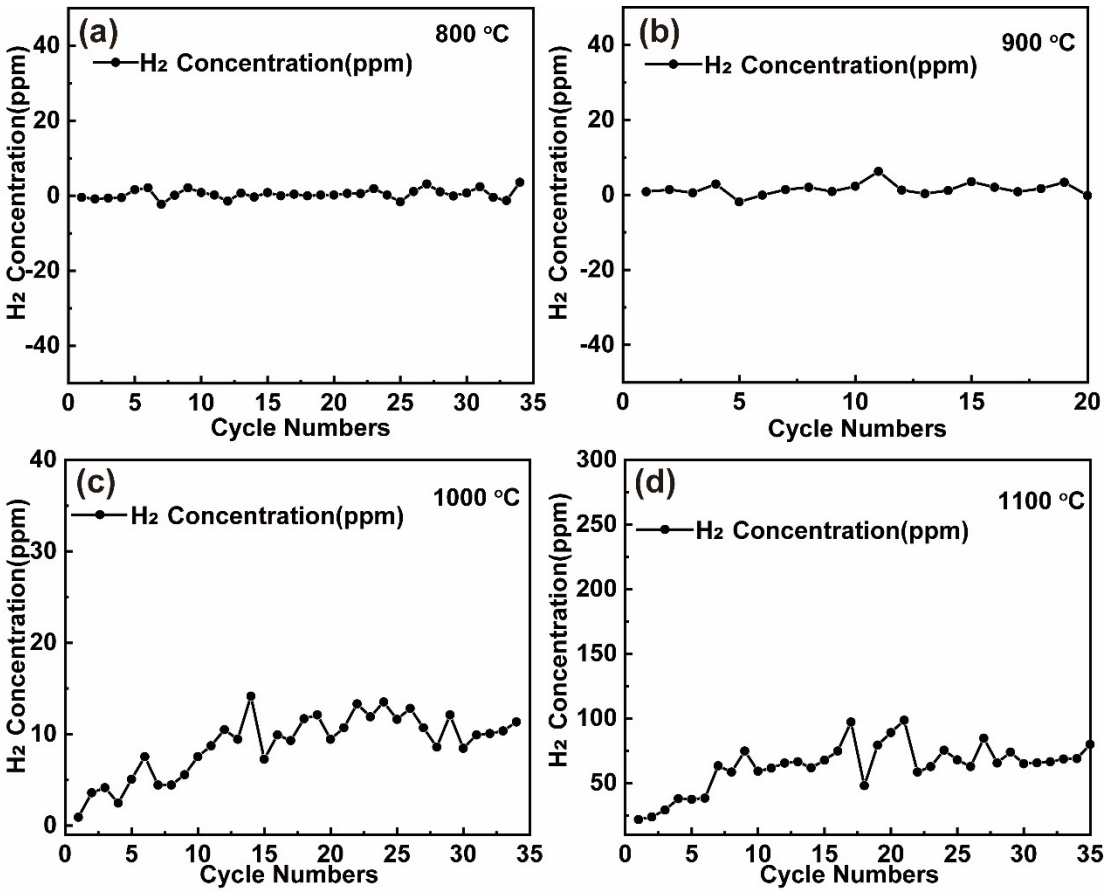

Figure S9 H_2 production from water thermolysis is catalyzed by LPNGSB_Mn and an alumina tube at (a) 800 °C, (b) 900 °C, (c) 1000 °C, and (d) 1100 °C.

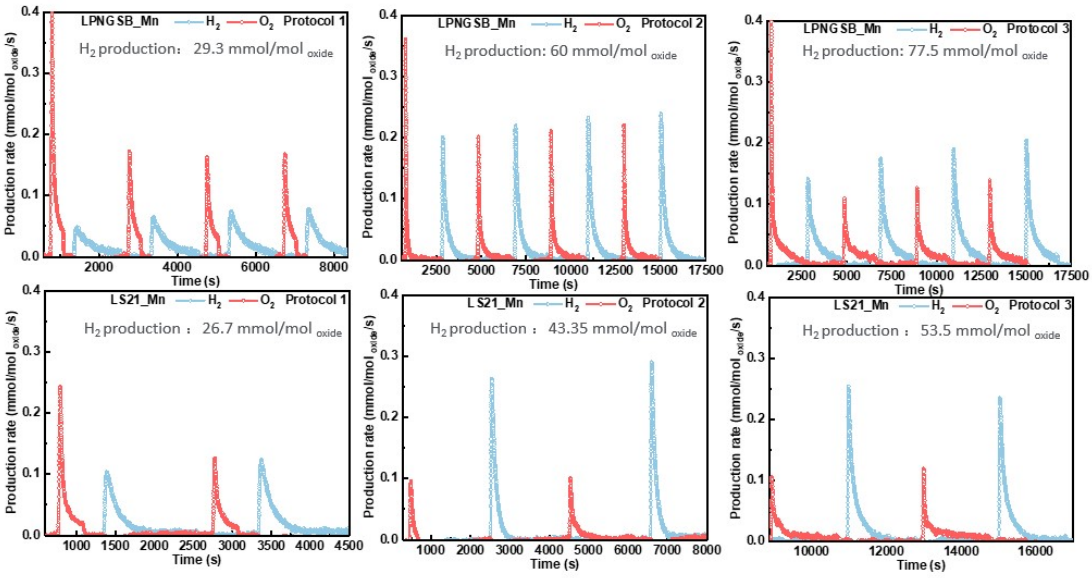

Figure S10 STCH results for LS21_Mn and LPNGSB_Mn. The specific test condition is shown **Table S4**. 'Protocol 1' will be referred to as 'P1', 'Protocol 2' as 'P2', and 'Protocol 3' as 'P3'. These protocols (P1, P2, P3) correspond to those in **Table 2**.

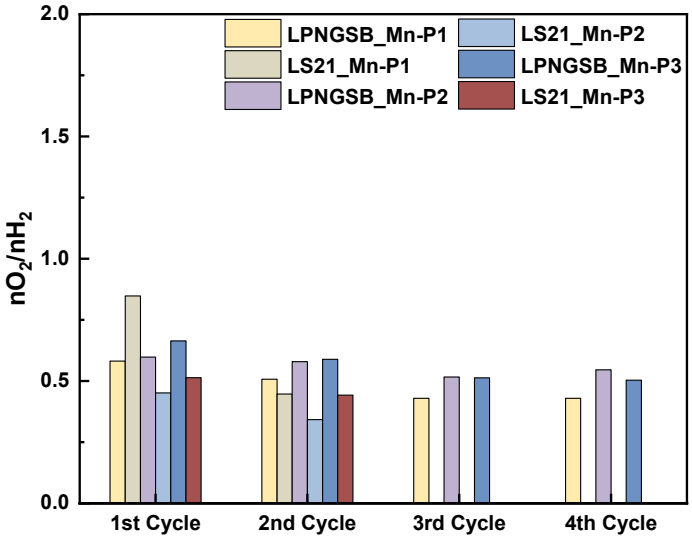

Figure S11 The molar ratio of O_2/H_2 for LS21_Mn and LPNGSB_Mn under different protocols.

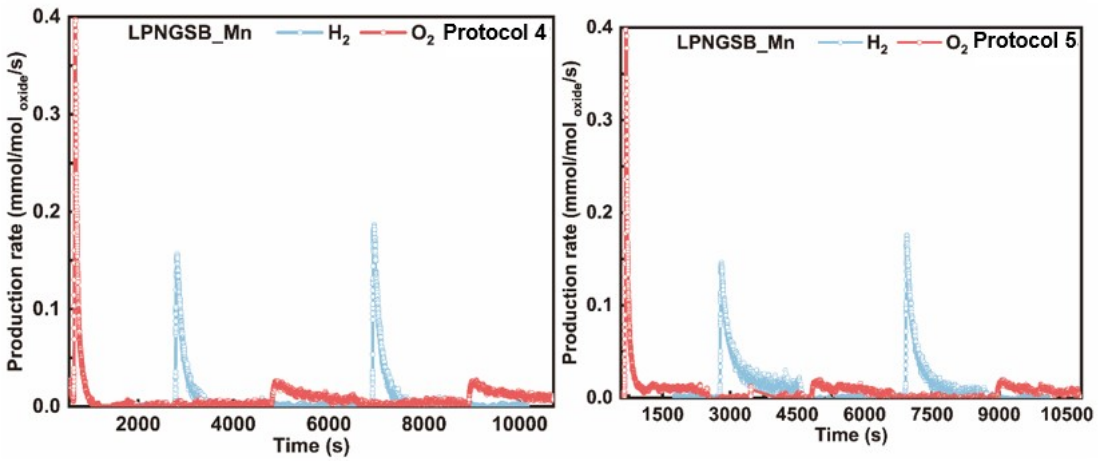

Figure S12 High-conversion (the molar ratio of H_2O and H_2 is 1000:1) water-splitting cycles for LPNGSB_Mn. The specific test condition is shown **Table S4**. The H_2 production of LPNGSB_Mn in the final cycle ranges from 5.58-10.2 mmol mol_{atom}^{-1} in protocol 4 (P4), and 15.5 mmol mol_{atom}^{-1} in protocol 5 (P5).

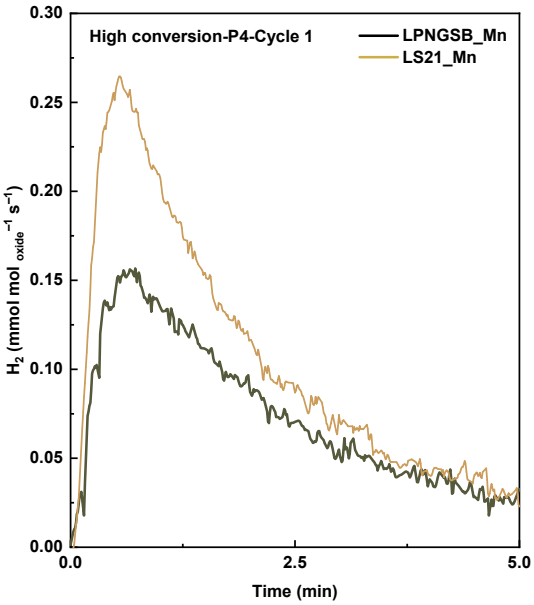

Figure S13 High-conversion water-splitting results, with a molar ratio of H_2O to H_2 of 1000:1 for LPNGSB_Mn and LS21_Mn. Detailed test conditions can be found in **Table S4**.

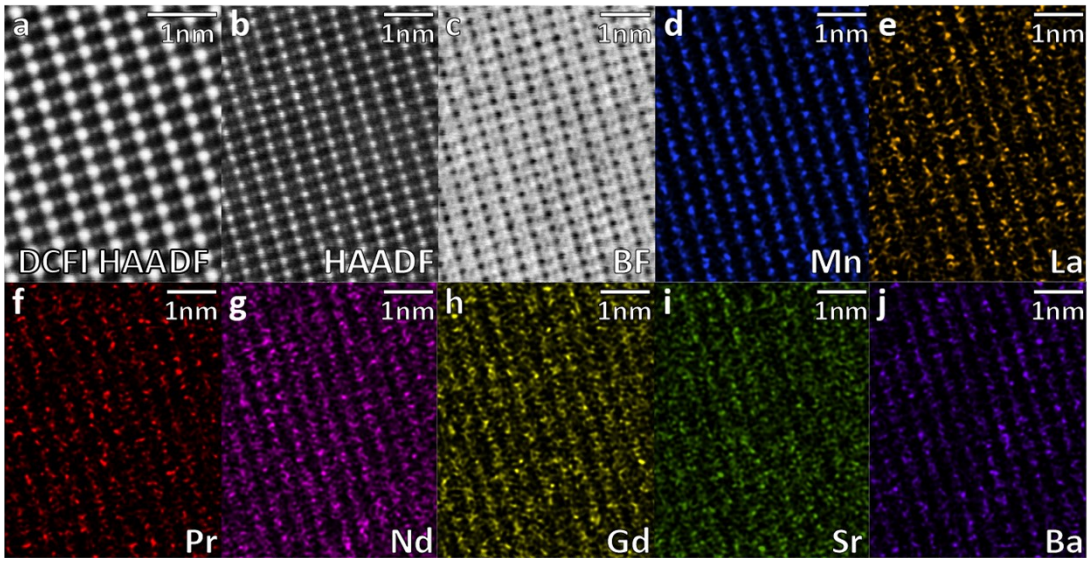

Figure S14 LPNGSB_Mn left in the reduced state (a) drift corrected frame integrated (DCFI) HAADF image showing A and B-site atoms as white and gray points of contrast respectively. (b) HAADF image (c) bright-field (BF) image (d) well-ordered Mn EDX map corresponding to the gray points of contrast in the HAADF image. (e) La EDX map (f) Pr EDX map (g) Nd EDX map (h) Gd EDX map (i) Sr EDX map and (j) Ba EDX map. (e-j) show atomic signals corresponding to the brightest white points in the HAADF images indicating a mixed species A-site occupation.

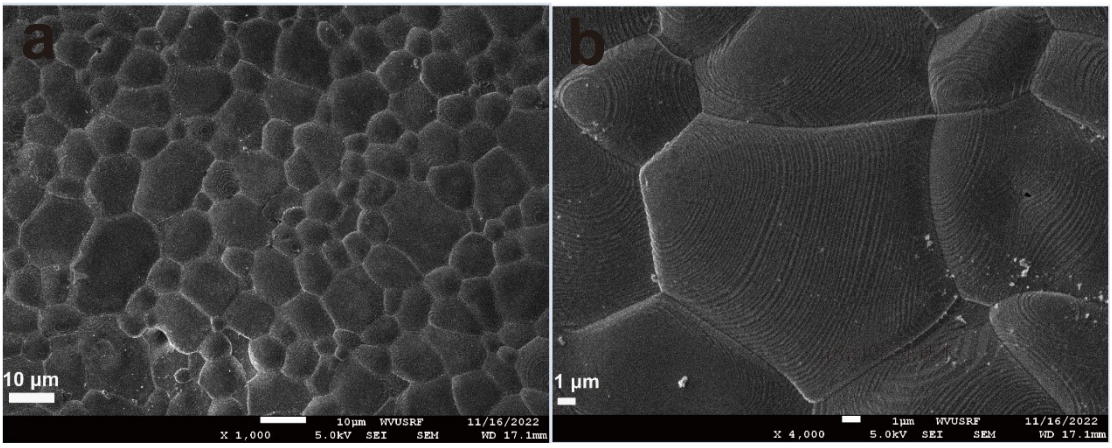

Figure S15 (a,b) SEM of ECR sample LPNGSB_Mn sintered at 1400 °C for 6 hours.

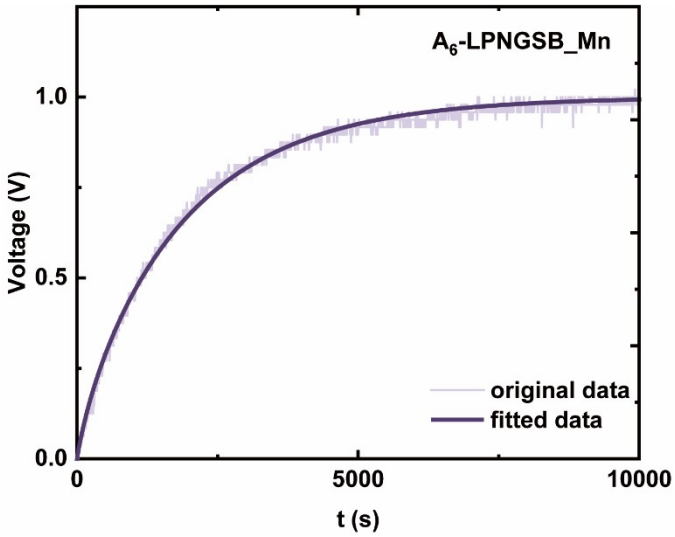

Figure S16 Electrical conductivity relaxation (ECR) result of LPNGSB_Mn.

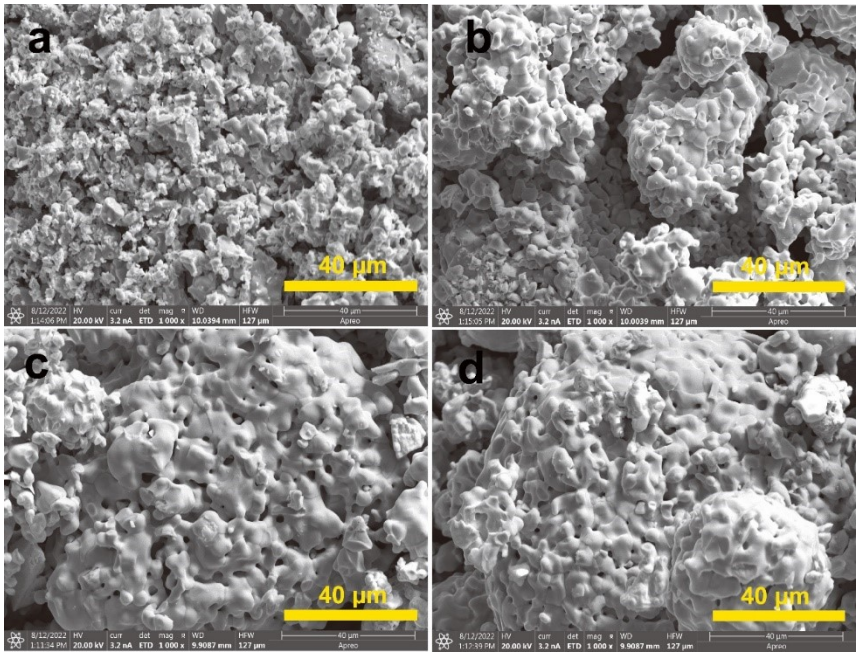

Figure S17 (a,b) low-magnification SEM images of the pristine sample $(La_{1/6}Pr_{1/6}Nd_{1/6}Gd_{1/6}Sr_{1/6}Ba_{1/6})MnO_3$ (LPNGSB_Mn) and (c,d) 50-cycled sample LPNGSB_Mn.

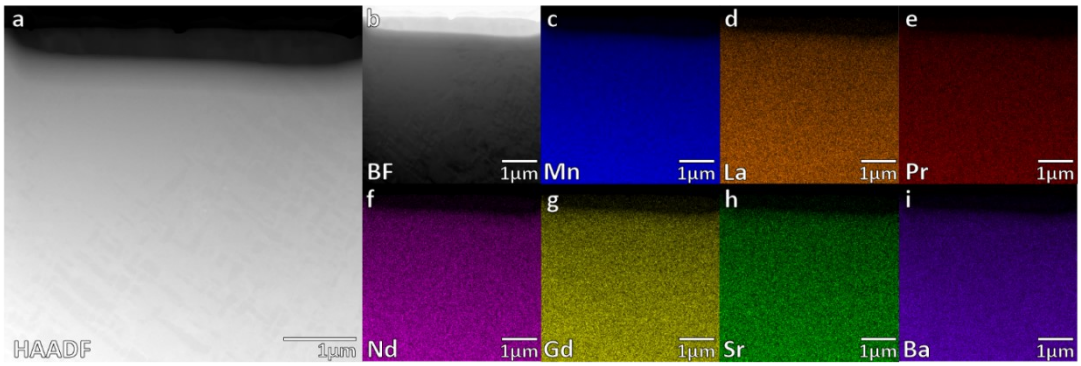

Figure S18 (a) HAADF-STEM image of the sample LPNGSB_Mn. (b) bright-field (BF) image. EDX mappings for elements: (c) Mn (blue), (d) La (orange), (e) Pr (red), (f) Nd (amaranth), (g) Gd (yellow), (h) Sr (green), (i) Ba (purple).

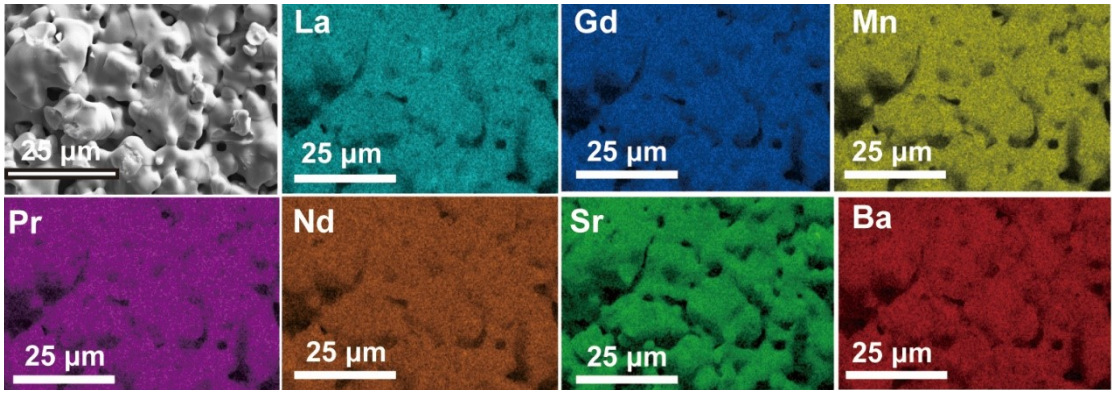

Figure S19 SEM images and corresponding EDX elemental maps are shown for the 50-cycled sample LPNGSB_Mn. The water-splitting cycles were conducted with reduction at 1350 °C and oxidation (water-splitting reaction) at 1100 °C for one hour.

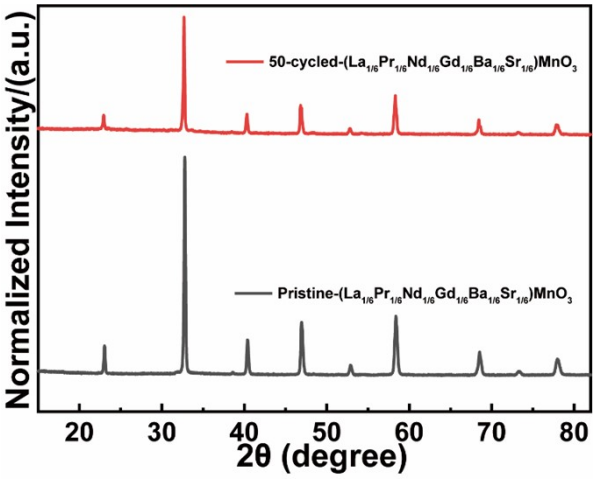

Figure S20 X-ray diffraction (XRD) patterns of pristine LPNGSB_Mn and 50-cycled LPNGSB_Mn.

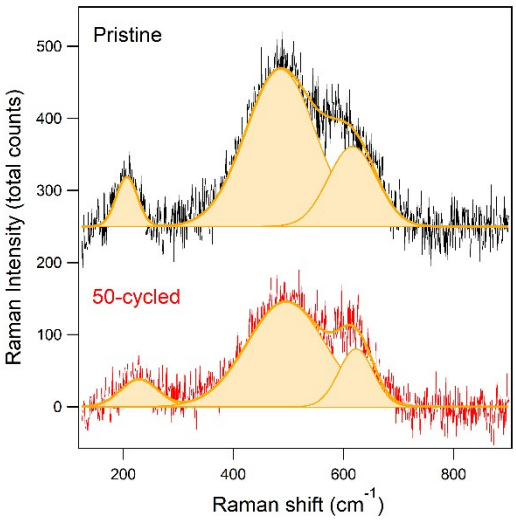

Figure S21 Raman spectra of pristine and 50-cycled LPNGSB_Mn.

Table S1. Lattice parameters were obtained by Rietveld refinements of X-ray diffraction (XRD) patterns of LS21_Mn and LPNGSB_Mn. Symbol * represents the sample after 50 STCH cycles.

sample	Lattice Parameter a (Å)	Lattice Parameter c (Å)	R_w(%)
LS21_Mn	5.50	13.36	6.82
LPNGSB_Mn	5.48	13.43	4.77
LPNGSB_Mn*	5.48	13.43	5.78

Table S2. Lattice parameters are adjusted in small-box modeling using PDFgui.

Samples	Lattice parameter a(Å)	Lattice parameter c(Å)
LS21_Mn	5.504	13.364

Table S3. STEM-EDX quantitative analysis of fresh LPNGSB_Mn displayed the average composition is 21.9±2.7 atom % Mn, 3.6±0.5 atom % Sr, 3.5±0.4 atom % Ba, 3.5±0.4 atom % La, 3.1±0.3 atom % Pr, 3.2±0.4 atom % Nd, 3.8±0.4 atom % Gd.

Element	Atomic Fraction (%)	Atomic Error (%)
Mn	21.9	2.7
Sr	3.6	0.5
Ba	3.5	0.4
La	3.5	0.4
Pr	3.1	0.3
Nd	3.2	0.4
Gd	3.8	0.4

Table S4. Testing protocols of LS21_Mn and LPNGSB_Mn for STCH.

Protocol	T_{red}/ T_{ox} (°C)	t_{red}/ t_{ox}(min)	Red/Ox atmosphere
P1	1350/1100	5/20	100% Ar/(40% H_2O/60% Ar)
P2	1350/1100	30/30	100% Ar/(40% H_2O/60% Ar)
P3	1350/900	30/30	100% Ar/(40% H_2O/60% Ar)
P4	1350/1100	30/30	100% Ar/ (0.04% H_2/39.68% H_2O/60.28% Ar)
P5	1350/900	30/30	100% Ar/ (0.04% H_2/39.68% H_2O/60.28% Ar)

Table S5. Summary of STCH production results of selected perovskite redox oxides tested at the reactor of Sandia National Laboratories.

Sample	T_{red}/ T_{ox} (°C)	t_{red}/ t_{ox}(min)	Gas Red/Ox	Cumulative H_2 production (μmol g^{-1})/(mmol mol_{oxide}^{-1})	Ref.
$BaCe_{0.25}Mn_{0.75}O_3$	1350/850	5.5/20	Ar/40% H_2O with Ar	140/36.6	[3]
$Sr_{0.4}La_{0.6}Mn_{0.6}Al_{0.4}O_3$	1350/850	5.5/20	Ar/40% H_2O with Ar	194/40.8	[3]
CeO_2	1350/850	5/20	Ar/40% H_2O with Ar	50/8.6	[3]
$Ca_{2/3}Ce_{1/3}Ti_{1/3}Mn_{2/3}O_3$	1350/850	5.5/20	Ar/40% H_2O with Ar	298.8/52	[4]
$(La_{1/6}Pr_{1/6}Nd_{1/6}Gd_{1/6}Sr_{1/6}Ba_{1/6})MnO_3$	1350/1100	5/20	Ar/40% H_2O with Ar	123.5/29.3	this work
$(La_{1/6}Pr_{1/6}Nd_{1/6}Gd_{1/6}Sr_{1/6}Ba_{1/6})MnO_3$	1350/1100	30/30	Ar/40% H_2O with Ar	252.8/60	this work
$(La_{1/6}Pr_{1/6}Nd_{1/6}Gd_{1/6}Sr_{1/6}Ba_{1/6})MnO_3$	1350/900	30/30	Ar/40% H_2O with Ar	326.6/77.5	this work

Table S6. Comparison of peak hydrogen production rates for different materials at 1100 °C and 900 °C across multiple cycles.

Material	$\dot{n}_{peak}$ (mmol mol $_{oxide}^{-1}$ s^{-1})-Cycle 1	$\dot{n}_{peak}$ (mmol mol $_{oxide}^{-1}$ s^{-1})-Cycle 2	$\dot{n}_{peak}$ (mmol mol $_{oxide}^{-1}$ s^{-1})-Cycle 3	$\dot{n}_{peak}$ (mmol mol $_{oxide}^{-1}$ s^{-1})-Cycle 4
LPNSGB_Mn-1100 °C	0.198	0.2185	0.2293	0.2374
LPNSGB_Mn-900 °C	0.1369	0.1728	0.1886	0.2021
LS21_Mn-1100 °C	0.2631	0.2892		
LS21_Mn-900 °C	0.2513	0.2343		

Table S7. STEM-EDX quantitative analysis of reduced LPNGSB_Mn displayed the average composition is 21.4±2.6 atom % Mn, 3.5±0.4 atom % Sr, 3.3±0.4 atom % Ba, 3.3±0.4 atom % La, 3.0±0.3 atom % Pr, 3.0±0.3 atom % Nd, 3.2±0.3 atom % Gd.

Element	Atomic Fraction (%)	Atomic Error (%)
Mn	21.4	2.6
Sr	3.5	0.5
Ba	3.3	0.4
La	3.3	0.4
Pr	3.0	0.3
Nd	3.0	0.3
Gd	3.2	0.3

Reference:

1. A. Riaz, T. Tsuzuki, F. Kremer, S. Sattayaporn, M. U. Ali, W. Lipinski and A. Lowe, *ACS Catal*, 2020, **10**, 8263-8276.
2. Y. H. Li, R. Gemmen and X. B. Liu, *J Power Sources*, 2010, **195**, 3345-3358.
3. D. R. Barcellos, M. D. Sanders, J. H. Tong, A. H. McDaniel and R. P. O'Hayre, *Energy Environ. Sci.*, 2018, **11**, 3256-3265.
4. R. B. Wexler, G. S. Gautam, R. T. Bell, S. Shulda, N. A. Strange, J. A. Trindell, J. D. Sugar, E. Nygren, S. Sainio, A. H. McDaniel, D. Ginley, E. A. Carter and E. B. Stechel, *Energy Environ. Sci.*, 2023, **16**, 2550-2560.